Supplementary Information

For

Mechanochemical reduction of clay minerals to porous silicon nanoflakes for high-performance lithium-ion battery anodes

Qingze Chen[a, b, c], Shoushu Wei[a, b, c], Runliang Zhu[a, b, c] *, Jing Du[a, b, c], Jieyang Xie[a, b, c], Haiming Huang[a, b, c], Jianxi Zhu[a, b, c], Zhengxiao Guo[d]

[a] *CAS Key Laboratory of Mineralogy and Metallogeny, Guangdong Provincial Key Laboratory of Mineral Physics and Materials, Guangzhou Institute of Geochemistry, Chinese Academy of Sciences, Guangzhou 510640, China*

[b] *CAS Center for Excellence in Deep Earth Science, Guangzhou 510640, China*

[c] *University of Chinese Academy of Sciences, Beijing 100049, China*

[d] *Department of Chemistry and HKU-CAS Joint Laboratory on New Materials, The University of Hong Kong, Hong Kong Island, Hong Kong SAR, China*

* Corresponding author

E-mail: zhurl@gig.ac.cn

Experimental Details

Materials

The raw talc used in this study was sourced from Liaoning, China. The sample was collected with a purity of over 99% for the following experiments after undergoing simple sedimentation and diluted acid leaching. The chemical composition was determined as follows: SiO_2 63.03%, MgO 32.20%, Al_2O_3 0.04%, Fe_2O_3 0.15%, Na_2O 0.04%, and the ignition loss 5.01%. Magnesium (Mg) was of analytical grade and supplied by Shanghai Maogon Nano Technology Co., Ltd. Both hydrochloric acid (HCl, 37 wt.%) and hydrofluoric acid (HF, 40 wt.%) were acquired from Guangzhou Chemical Reagent Factory.

Materials synthesis

The porous silicon nanoflakes (PSNs) were synthesized via a simple mechanochemical reduction method. In a typical procedure, talc and Mg powders as starting materials were mixed in a mass ratio of 1:0.6, and transferred into a stainless-steel vial (500 mL) in an argon-filled glovebox. The milling steel balls with a diameter of 10 mm were added to the vial in a ball-to-powder mass ratio of 20:1. The vial was securely sealed and placed in a planetary ball mill (YXQM-4L, Changsha MITR Instrument, China) which was then operated at 700 rpm for 3 h. After cooling down naturally, the as-milled mixtures were treated with HCl for 3 h in order to remove the byproducts MgO, followed by leaching with 1% HF. Subsequently, the resulting PSNs were thoroughly washed with ethylalcohol and distilled water, vacuum-dried overnight at 60°C, and collected for further experiments. For the control experiment, talc was treated with sulfuric acid to eliminate the octahedral

sheets. Then the resulting silica was used as the Si precursor instead of talc for synthesizing the Si particles (SPs) with a silica/Mg mass ratio of 1:0.8 under the same mechanical milling conditions.

Characterization

Powder X-ray diffraction (XRD) patterns of the samples were determined by utilizing a Rigaku MiniFlex-600 X-ray diffractometer with CuKα radiation (λ = 0.154 nm) at an energy of 40 kV and a current of 15 mA. Scanning electron microscopy (SEM) images and energy-dispersive X-ray spectroscopy (EDS) patterns were observed through a Hitachi SU-8010 cold field scanning electron microscope. Transmission electron microscopy (TEM) images and EDS pattern were acquired with an FEI Talos F200S field-emission transmission electron microscope with an energy dispersive spectrometer at an acceleration voltage of 200 kV. Raman spectra were collected on a HORIBA XploRA PLUS confocal micro-Raman spectrometer with an Ar-ion laser (λ = 532 nm). X-ray photoelectron spectroscopy (XPS) spectra were recorded on a Thermo Scientific K-Alpha XPS system with a monochromatic Al-Kα X-ray source (1468.6 eV). The N_2 adsorption-desorption isotherm of the sample was recorded using the Micromeritics ASAP 2020 instrument at liquid nitrogen temperature (−196°C). The specific surface area was calculated based on the multi-point Brunauer-Emmett-Teller method, and the total pore volume was evaluated from the N_2 adsorption capacity at a relative pressure of 0.97. The pore size distribution pattern was determined by the Barrett-Joyner-Halenda (BJH) method.

Electrochemical measurements

To evaluate the electrochemical performance of the samples (e.g., PSNs and SPs), CR2032

coin-type half cells were assembled in an Ar-filled glovebox with both H_2O and O_2 levels below 0.1 ppm. The working electrode of the Si-based anode was prepared by employing an aqueous slurry coating approach: a mixture of the Si material, sodium alginate (SA) binder, and conductive Super P in a mass ratio of 70:15:15 with distilled water as the solvent was uniformly blade-coated onto the copper foil, vacuum-dried at 80°C overnight, and then cut into the circular electrodes. The mass loading of active material was 0.6-1.5 mg cm^{-2}. The lithium foils served as both counter and reference electrodes, and the Celgard 2500 microporous polyethylene membranes as separators. The electrolyte was a mixture of 1 M $LiPF_6$ in ethylene carbonate/dimethyl carbonate (EC/DMC in a 1:1 volume ratio) with 10 wt.% fluoroethylene carbonate (FEC). A CHI660E electrochemical workstation was employed for cyclic voltammetry (CV) measurements at a scan rate of 0.1 mV s^{-1} and electrochemical impedance spectroscopy (EIS) tests with an AC voltage of 5 mV in the frequency range of 0.01-100 kHz. A LAND-CT2001A multichannel battery-testing instrument was used to test the cycling stability and rate capability of the electrodes within a voltage window of 0.01-1.5 V. The gravimetric capacity was calculated based on active materials only. The electrode was relaxed for 20 min after a pulse current of 0.2 A g^{-1} for 10 min for the galvanostatic intermittent titration technique (GITT) test. After electrochemical measurements, the cycled cells were carefully disassembled in an Ar-filled glovebox and the working electrodes were completely washed with acetonitrile for further characterization.

The full cells were manufactured using a PSNs anode and commercial $LiCoO_2$ (LCO) cathode with a negative electrode capacity/positive electrode capacity (N/P) ratio of 1.1:1.0. The cathode was composed of LCO, polyvinylidene fluoride binder, and Super P in a mass

ratio of 80:10:10 on aluminum foil. Before being assembled into full cells, the PSNs electrodes were pre-lithiated by being in contact with a lithium foil for 20 min with the electrolyte between them. The full cells were fabricated under the same conditions as the half cells. The electrochemical performance of the full cell was measured in a voltage window of 2.75-4.35 V.

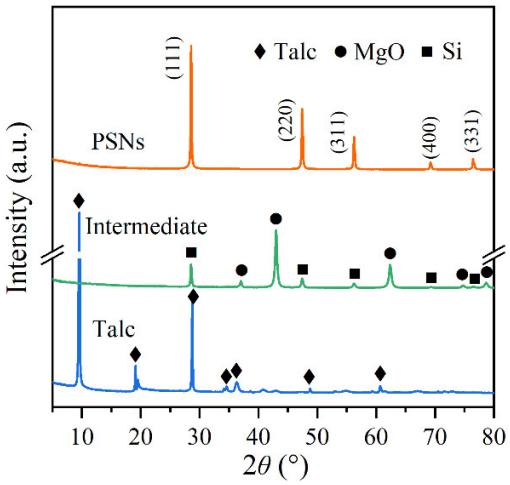

Figure S1. XRD patterns of the precursor talc, the intermediate after reduction reaction, and the resulting porous silicon nanoflakes (PSNs) after acid treatment.

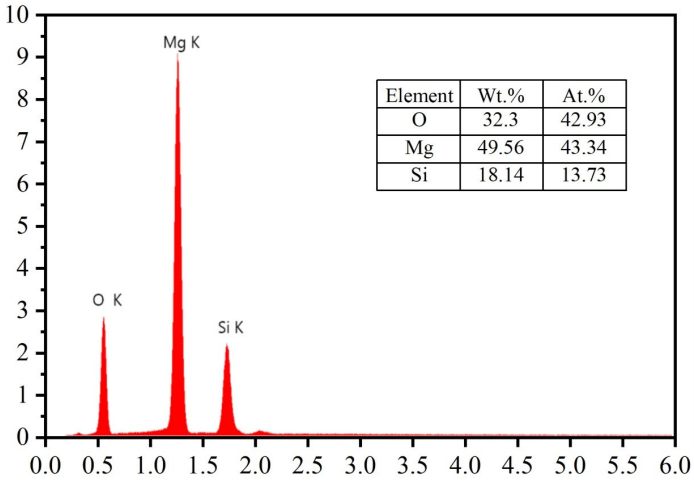

Figure S2. SEM-EDS pattern of the intermediate after mechanochemical reduction of talc.

SEM-EDS pattern of the intermediate exhibited the co-existence of Mg, O, and Si (Figure S2). The intermediate only contained MgO and Si (as shown by the XRD pattern in Fig. S1), and the atomic ratio of Mg/O was about 1 (corresponding to MgO). Therefore, Si content in the intermediate was 18.14 wt%. In a typical procedure, 10 g talc and 6 g Mg powders were used as initial reactants. The Si amount in the intermediate was calculated to be 2.90 g (= 18.14%*(10+6) g), which was close to the theoretical value of 2.94 g (= 10*63.03%*28/60 g). The final Si product after acid washing was weighed to be 2.73 g, corresponding to the Si yield of ~93% according to the following equation:

$$w = 100*m_f/m_t$$

where w represents the yield of the Si product; m_f and m_t represent the final actual Si and the theoretical Si amount in the original talc, respectively.

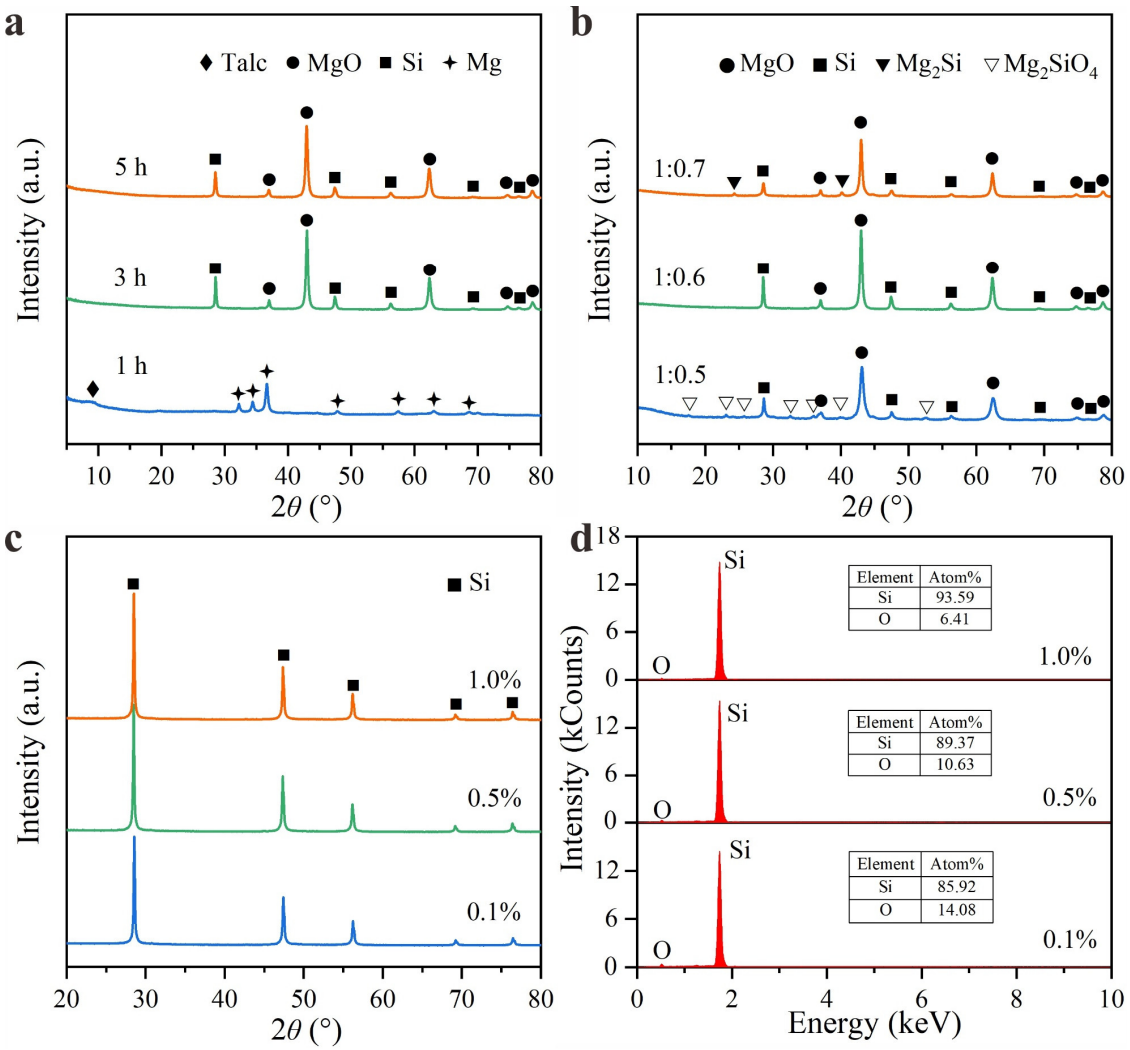

Figure S3. XRD patterns of the intermediates (after mechanochemical reduction of talc) obtained for various mechanical milling times (the mass ratio of talc/Mg: 1:0.6) (a) and at various mass ratios of talc/Mg (mechanical milling time: 3h) (b). XRD patterns (c) and SEM-EDS patterns (d) of the final Si products obtained by using various concentrations of HF. Other experimental conditions remained the same as those for the synthesis of PSNs if not otherwise specified.

XRD patterns of the intermediate obtained by milling for 1 h showed the reflections of Mg and talc, while those for 3 h and 5 h exhibited the reflections of MgO and Si (Fig. S3a). The results indicated that the short-time ball milling was unable to achieve the reduction

of clay mineral and the magnesiothermic reduction could be initiated only when the accumulated heat from the mechanical milling was sufficient to surmount the reaction activation barrier.

XRD patterns of the intermediate obtained at a talc/Mg mass ratio of 1:0.5 exhibited the typical reflections of Mg_2SiO_4 besides MgO and Si, while that at a talc/Mg mass ratio of 1:0.7 showed Mg_2Si besides MgO and Si (Fig. S3b). When the talc/Mg mass ratio was set as 1:0.6, there were hardly any other visible Si-containing byproducts, thus leading to a high yield of the final Si product.

To investigate the influence of HF on the removal efficiency of oxide components on Si, 150 mg product (after acid washing by HCl) was treated with 40 mL HF with various concentrations (0.1%, 0.5%, and 1.0%). The XRD patterns of all the final Si products exhibited similar reflections of Si (Fig. S3c). Moreover, SEM-EDS patterns of the final Si products showed that the oxide contents decreased with the concentrations of HF increasing (Fig. S3d). The oxide content could decrease to 6.41% with 1.0% HF used.

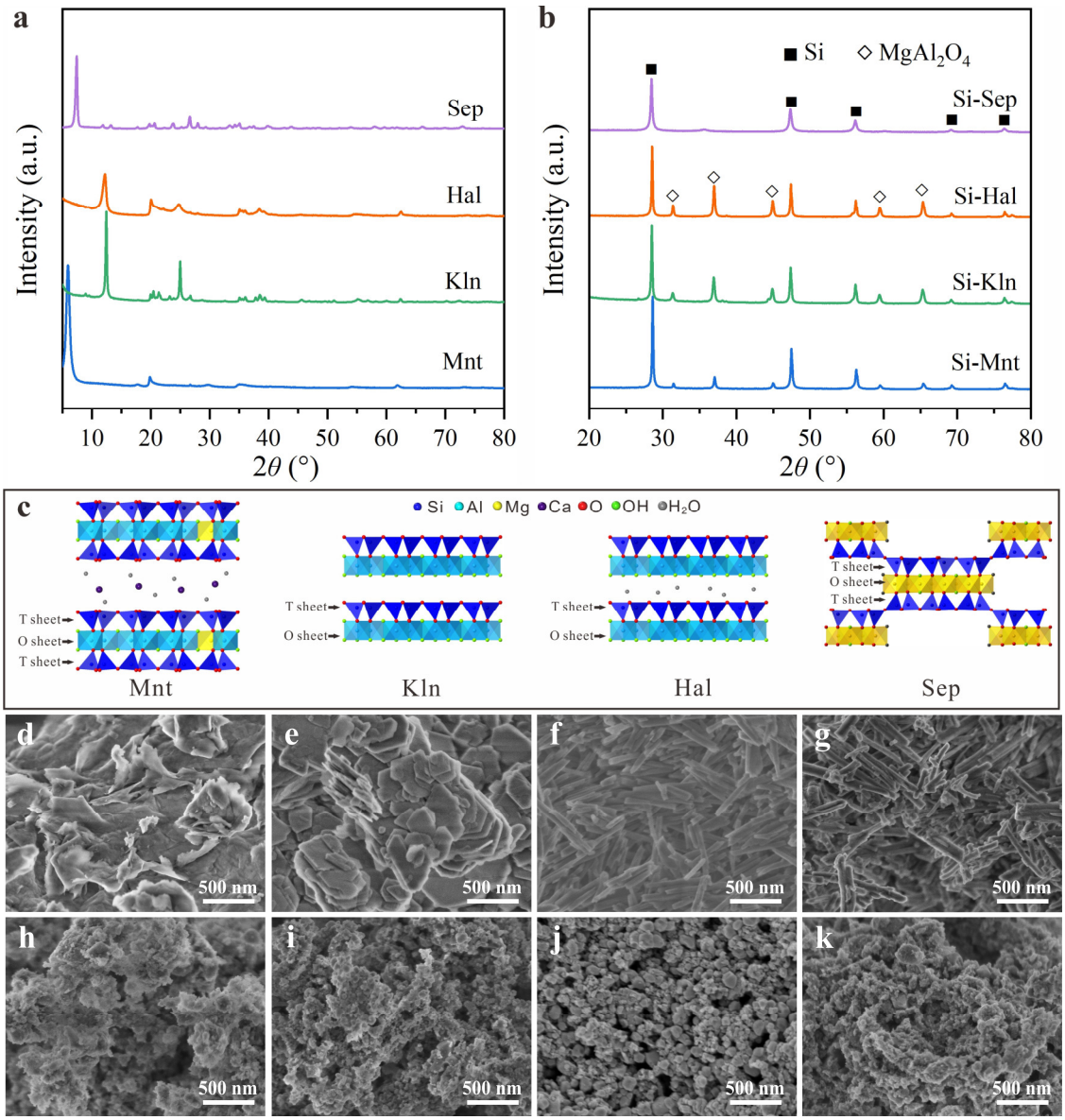

Figure S4. XRD patterns of clay minerals (montmorillonite (Mnt), kaolinite (Kln), halloysite (Hal), and sepiolite (Sep)) (a) and the corresponding final Si products obtained by the mechanochemical reduction strategy (Si-Mnt obtained at 700 rpm for 3 h, Si-Kln obtained at 700 rpm for 9 h, Si-Hal obtained at 700 rpm for 12 h, and Si-Sep obtained at 700 rpm for 3 h) (b). (c) Crystal structures of clay minerals (the individual layers of clay minerals mainly consist of a tetrahedral (T) sheet and an octahedral (O) sheet in either a 1:1 (TO type, e.g., Kln and Hal) or 2:1 (TOT type, e.g., Mnt and Sep) proportion). SEM

images of clay minerals (Mnt (d), Kln (e), Hal (f), and Sep (g)) and the corresponding final Si products (Si-Mnt (h), Si-Kln (i), Si-Hal (j), and Si-Sep (k)).

Three Al-containing clay minerals (Mnt, Kln, and Hal) and one Mg-containing clay mineral (Sep) were used as precursors for the synthesis of Si products via the mechanochemical reduction strategy (Fig. S4a). Before the reduction reaction, the clay minerals were heated at 400°C for 2 h to remove the adsorbed water (which could react with Mg powders). Based on the chemical compositions of the clay minerals (Table S1), the used mass ratios of clay/Mg were set as 1:0.70, 1:0.75, 1:0.75, and 1:0.55 for the Mnt, Kln, Hal, and Sep systems, respectively.

Our results showed that Mnt and Sep could be reduced in only 3 hours, while Kln and Hal needed 9 h and 12 h at the same rotation speed of milling (700 rpm). Compared with Kln and Hal, Mnt and Sep possessed more Si content (Table S1) and TOT-type structure (Fig. S4c), which could increase the contact/reaction probability between silicon-oxygen tetrahedra and Mg. The XRD patterns of Al-containing clay-derived Si products exhibited the characteristic reflections of spinel $MgAl_2O_4$ besides Si in comparison to that of Mg-containing clay-derived Si product (Fig. S4b). Moreover, the spinel contents of Si products increased with the Al contents of clay minerals increasing. SEM images showed that Si-Mnt exhibited a lamellar and porous structure (Fig. S4h), somewhat maintaining the original 2D structure of Mnt (Fig. S4d). By contrast, the other three Si products showed a loose texture composed of nanoparticles (Fig. S4e-g), different from their precursors (Fig. S4i-k), which could be attributed to the structure damage by prolonged mechanical action (for Si-Kln and Si-Hal) and the poor resistance of one-dimensional structures to ball milling (for Si-Sep). The above results indicated that various clay minerals (including Mnt, Kln,

Hal, and Sep) could be reduced into nanostructured Si via the mechanochemical reduction strategy, and the properties of the clay minerals had a great influence on the structure and morphology of the final Si products.

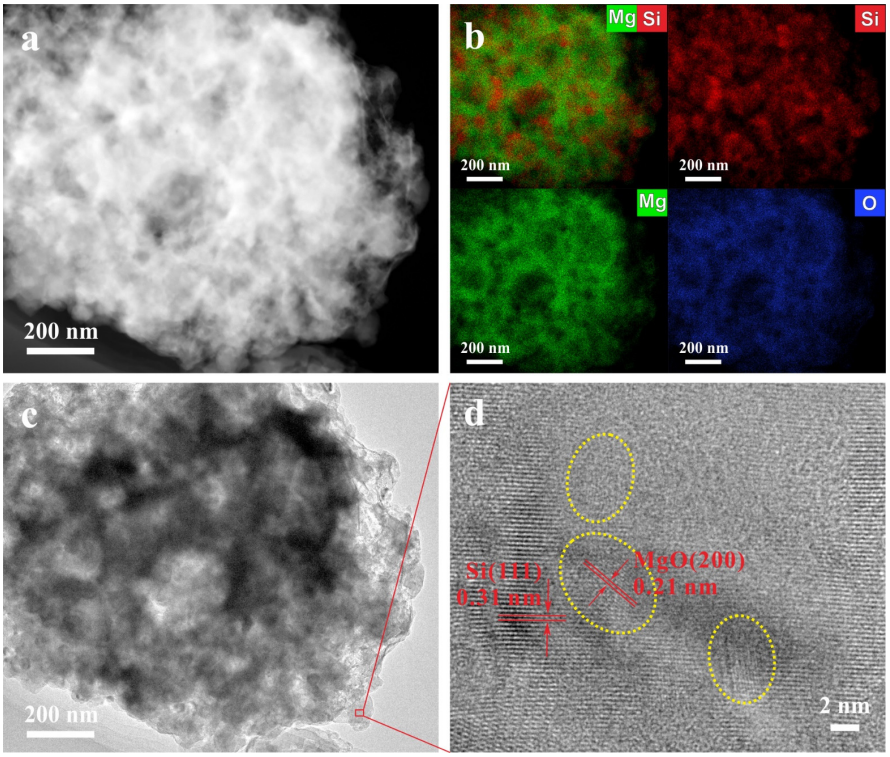

Figure S5. Dark-field TEM image (a), the corresponding EDS mapping (b), TEM image (c), and HRTEM image (d) of the intermediate after mechanochemical reduction of talc (without acid washing). The yellow circles represent the MgO zones that were embedded in the Si zones.

The EDS mapping indicated that Mg (O) and Si were distributed in a staggered manner on the intermediate. Furthermore, the HRTEM image showed that the MgO nanocrystals were embedded in the Si substrate. These MgO nanoparticles could be removed by acid washing, forming the hierarchical porous architecture of PSNs.

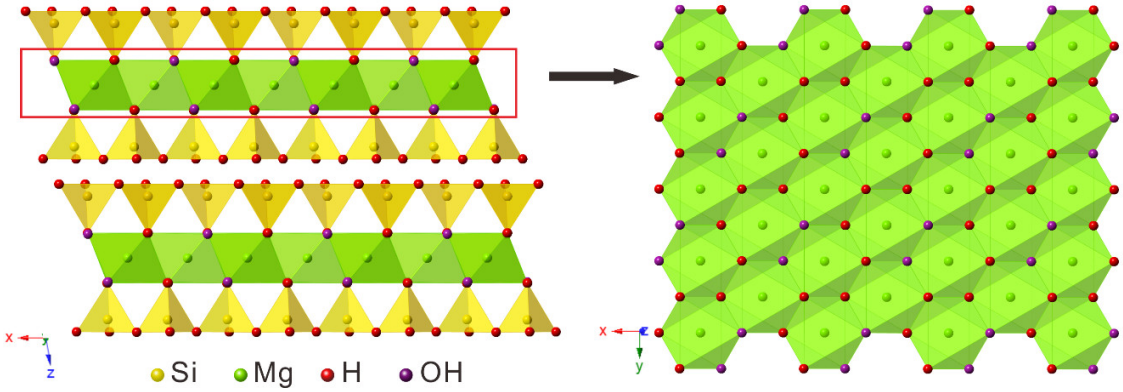

Figure S6. The crystal structure and the corresponding octahedral sheets (top views) of talc. The magnesium-oxygen/hydroxide octahedral sheet could scavenge heat through its decomposition reaction ($Mg(OH)_2$ (s) → MgO (s) + H_2O (g); ΔH = 80.5 kJ/mol $_{Mg(OH)2}$).

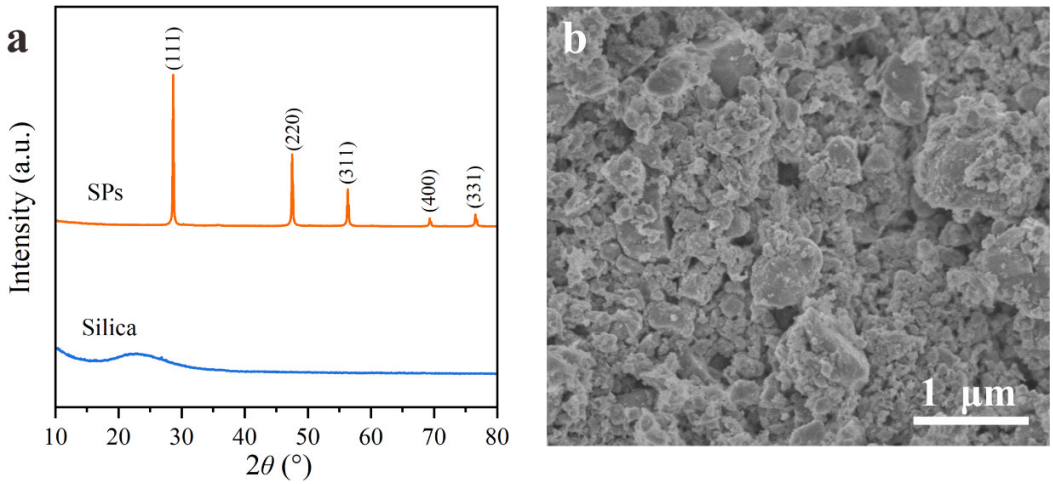

Figure S7. (a) XRD patterns of silica obtained by washing talc with sulfuric acid and the final silicon products (SPs) from the mechanochemical reduction of silica. (b) SEM image of SPs.

The acid washing removed the octahedral sheets of talc, leading to the formation of amorphous silica, as evidenced by a broad diffraction peak at ~22.5° (2θ) in the XRD pattern (Fig. S7a). The mechanochemical reduction process converted the amorphous silica into crystalline Si particles (SPs), which displayed similar characteristic reflections to PSNs. However, quite different from the nano-flaked morphology of the PSNs, the SPs presented severely agglomerated particles with irregular shapes (Fig. S7b). The results indicated that the reaction temperature during the reduction of silica was higher than that of talc, which was attributed to the lack of heat scavenger (octahedral sheets). Moreover, without octahedral sheets acting as effective templates, Si products tended to form random structures under mechanical milling.

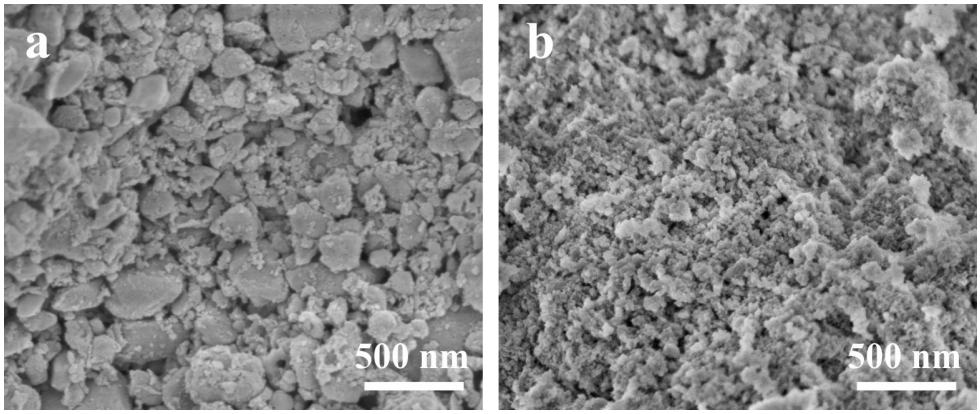

Figure S8. SEM images of the final Si products from the mechanochemical reduction (700 rpm, 6 h) of amorphous silica (obtained by removing the octahedral sheets of talc with sulfuric acid) (a) without and (b) with the introduction of MgO and $Mg(OH)_2$.

To verify the role of MgO and $Mg(OH)_2$ during the mechanochemical reduction process, a control experiment using a mixture of amorphous silica, Mg, MgO, and $Mg(OH)_2$ as initial reactants was carried out. In a typical procedure, the mass ratio of amorphous silica, Mg, MgO, and $Mg(OH)_2$ was set as 0.63:0.21:0.16:0.6, which was based on the chemical composition of talc (SiO_2 63.03%, MgO 32.20%, and the ignition loss 5.01%.). The mechanical milling time was set as 6 h to ensure that the reduction reaction could take place since the introduction of MgO and $Mg(OH)_2$ decreased the contact/reaction probability between silicon-oxygen tetrahedra and Mg. For comparison, the silica system without MgO and $Mg(OH)_2$ was carried out under the same mechanical milling conditions (6h). The SEM images showed that Si products from the system with the introduction of MgO and $Mg(OH)_2$ exhibited significantly reduced sizes (Fig. S8b) in comparison to that from the single silica system (Fig. S8a). These results demonstrated that MgO and $Mg(OH)_2$ could act as heat scavengers like the magnesium-oxygen/hydroxide octahedra, thus decreasing the system temperature during the magnesiothermic reduction process and hindering the formed Si nanocrystals from aggregating into bulk particles.

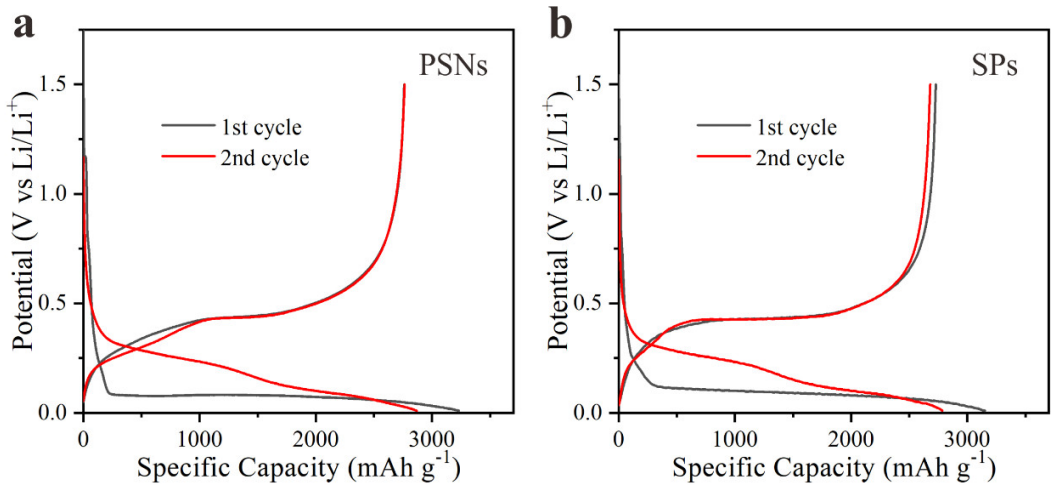

Figure S9. Discharge-charge curves of the PSNs (a) and SPs (b) electrodes at a current density of 0.2 A g^{-1}.

The PSNs electrode exhibited an initial Coulombic efficiency (CE) of 85%, slightly lower than that of SPs (87%) (Fig. S9), which was mainly attributed to the larger specific surface area (facilitating the formation of SEI films and consequently increased the irreversible capacity loss). Both the SEM-EDS pattern (Fig. S3d) and the TEM-EDS pattern (Fig. 2f) confirmed the small amount of oxygen in the Si product. The oxygen would increase the irreversible phases Li_2O and Li_4SiO_4 during the initial charge/discharge process,[1, 2] thus lowering the ICE of the Si product. On the other hand, Si nanoparticles with very small size (as shown by TEM images in Fig. 2c-d) were inevitably formed under mechanical milling, which may increase the specific surface area of the Si product and thus further harm the ICE. Although inferior to the ICE of SPs, that of PSNs still reached 85%, which was comparable to or better than those of the recently reported Si-based anodes (Table S2).

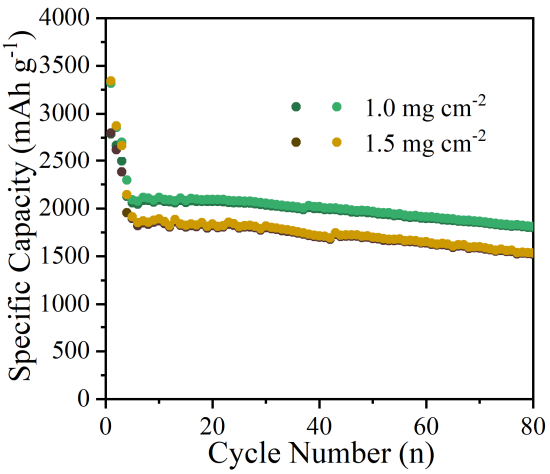

Figure S10. Cycling performances of the PSNs electrodes with active mass loadings of ~1.0 and 1.5 mg cm^{-2} at current densities of 0.2 A g^{-1} for the first three cycles and 1.0 A g^{-1} for the following cycles.

The PSNs electrode with an active mass loading of ~1.0 mg cm^{-2} delivered a high reversible capacity of ~1800 mAh g^{-1} at 1.0 A g^{-1} after 80 cycles, with a capacity retention of 85%. When the active mass loading was increased to 1.5 mg cm^{-2}, the electrode still maintained a reversible capacity of ~1522 mAh g^{-1} at the same test conditions, demonstrating its impressive cycling stability (even with a relatively high active mass loading).

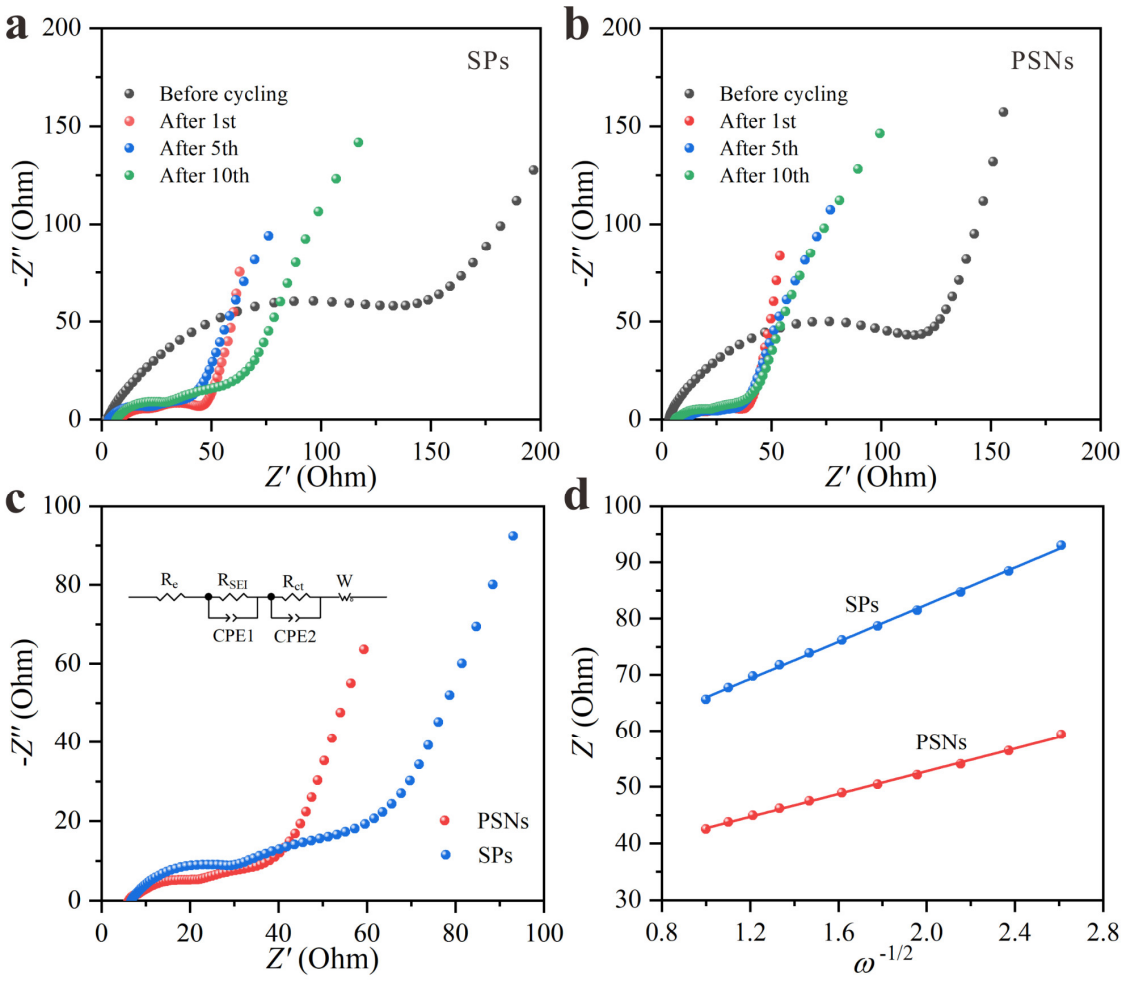

Figure S11. Nyquist plots of the SPs (a) and PSNs (b) electrodes before and after cycling for different cycles. (c) Nyquist plots of the SPs and PSNs electrodes after 10 cycles along with the equivalent circuit diagrams (R_e denotes the electrolyte resistance; R_{SEI} denotes the resistance in the SEI film interface; R_{ct} denotes the charge transfer resistance in the electrode-electrolyte interface; W denotes the Warburg impedance for the diffusion of lithium ions; CPE1 and CPE2 denote the resistors with constant phase elements). (c) The relationship between Z' and $\omega^{-1/2}$ in the low-frequency region.

As shown by the Nyquist plots, the PSNs electrode before cycling exhibited a smaller high-frequency semicircle than the SPs electrode (Fig. S11a and b), indicating a lower charge

transfer resistance of the former. Furthermore, the high-frequency semicircles of the PSNs electrodes after 1, 5, and 10 cycles showed similar characteristics, while those of the SPs electrodes displayed distinct differences. These results suggested that the PSNs electrode possessed better interfacial stabilization during electrochemical reaction.

According to the fitted data from the equivalent circuit, the R_{SEI} and R_{ct} values of the PSNs electrodes after 10 cycles were 18 and 26 Ω, respectively (Fig. S11c), which were smaller than those of the SPs electrode (25 and 31 Ω). The lower charge/Li^+ interfacial transfer resistances suggested the faster ion/electron transfer kinetics for the PSNs electrode. Furthermore, the diffusivity of lithium ions was inversely proportional to the slope of the curve between Z' and $\omega^{-1/2}$ in the low-frequency region (known as the Warburg coefficient, σ_w).[3] The σ_w values for the PSNs and SPs electrodes were 10 and 17 Ω $s^{-1/2}$, respectively (Fig. S11d). The PSNs electrode showed a smaller σ_w, demonstrating a better diffusion of lithium ions.

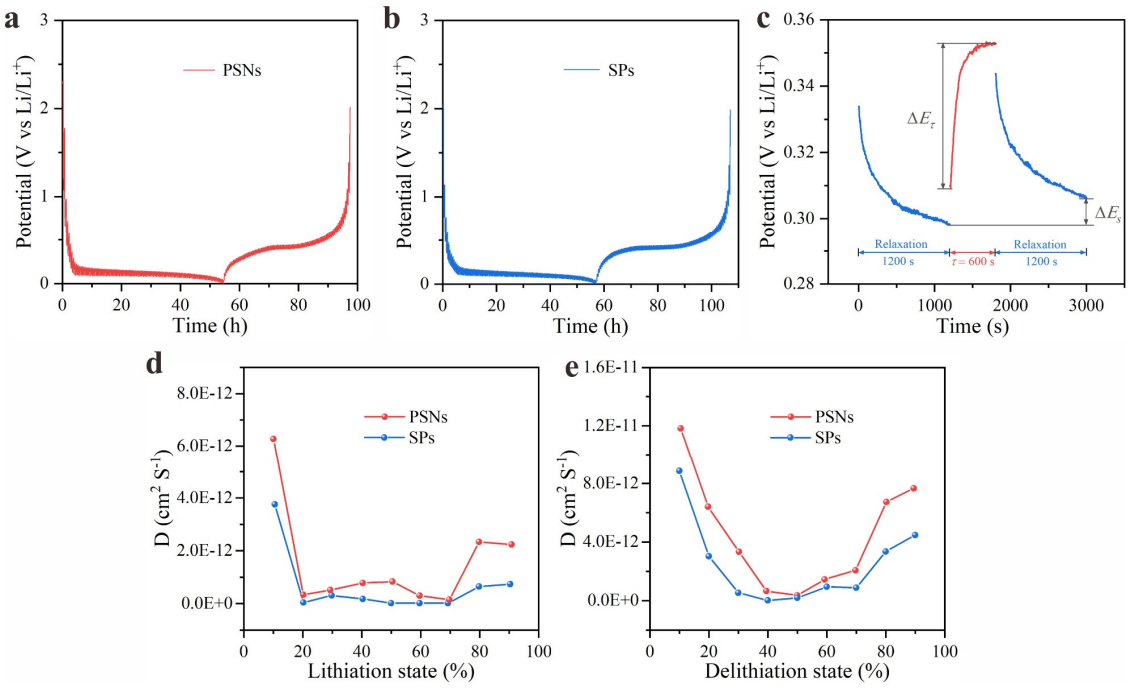

Figure S12. GITT curves of the PSNs (a) and SPs (b) electrodes. (c) The potential-time curves during the charge and relaxation processes in a selected period of the GITT curve. Li^+ diffusion coefficients in the discharged (d) and charged (e) states of the PSNs and SPs electrode.

The Li^+ diffusion coefficients (D_{Li}) of the electrodes can be calculated by the following simplified equation[4, 5]:

$$D_{\mathrm{Li}} = \frac{4}{\pi\tau}\left(\frac{m_B V_M}{M_B S}\right)^2 \left(\frac{\Delta E_s}{\Delta E_\tau}\right)^2$$

where m_B, M_B, V_M is the mass, molar mass, and molar volume of electrode material, respectively; S represents the electrode−electrolyte interface area; the τ, ΔEs, and $\Delta E\tau$ stand for the constant current pulse time, the voltage change during the open circuit period, and the voltage change during the constant current pulse, which could be obtained from the GITT curves (Figure. S12). As shown in Fig. 4d-e, the D_{Li} of the PSNs electrode at various discharge and charge states were larger than those of the SPs electrode, clearly

demonstrating the more efficient Li^+ diffusion during the lithiation/delithiation processes of PSNs. These results could be attributed to the synergistic effect of the nanoflake morphology and the hierarchical porosity of the PSNs.

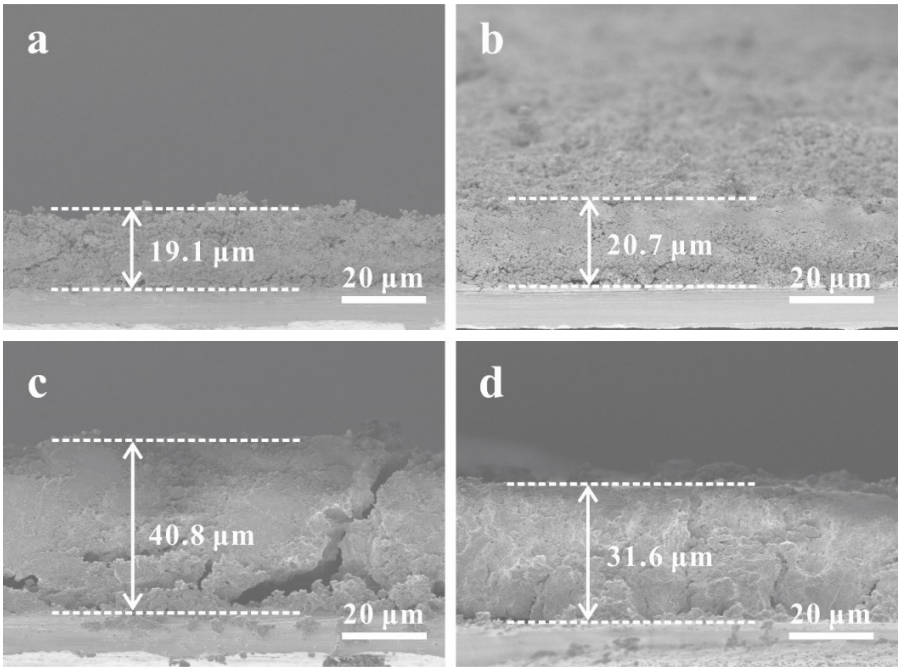

Figure S13. Cross-sectional SEM images of the SPs (a, c) and PSNs (b, d) electrodes before electrochemical tests (a, b) and after 100 cycles at 1.0 A g^{-1} (c, d).

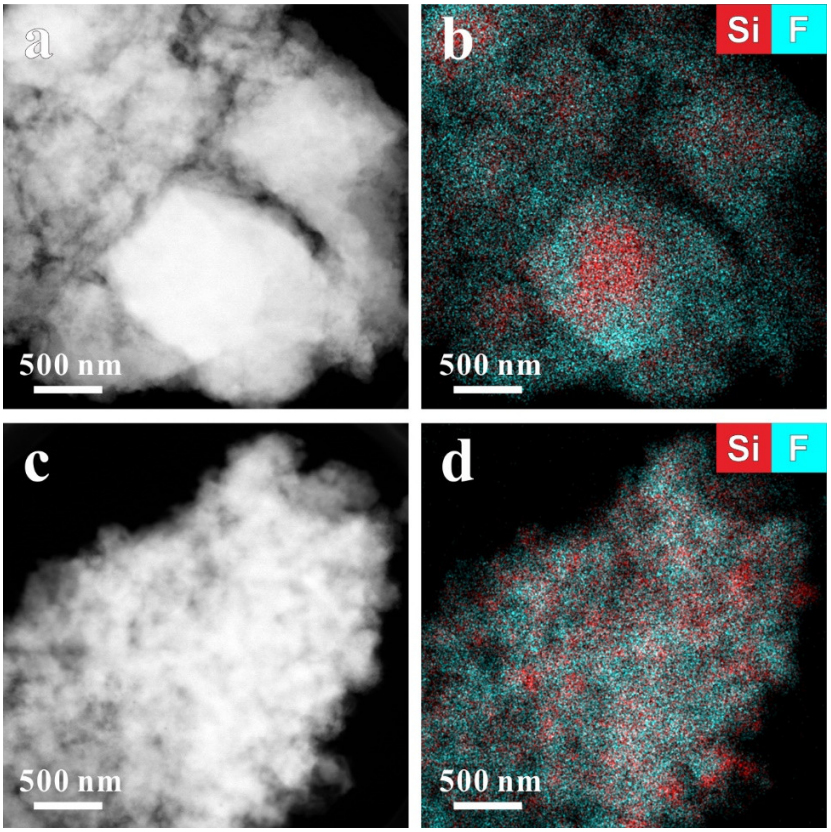

Figure S14. Dark-field TEM images and EDS mapping of SPs (a and b) and PSNs (c and d) after 100 cycles at 1.0 A g^{-1}.

Dark-field TEM images showed that PSNs kept a relatively intact morphology in comparison to SPs after cycling. Furthermore, EDS mapping revealed that Si and F were more evenly distributed on PSNs than SPs, and that the F coating on the Si of PSNs was thinner than that of SPs, suggesting the thinner generated SEI films on PSNs. The results indicated that PSNs had superior structural and interfacial stability during cycling.

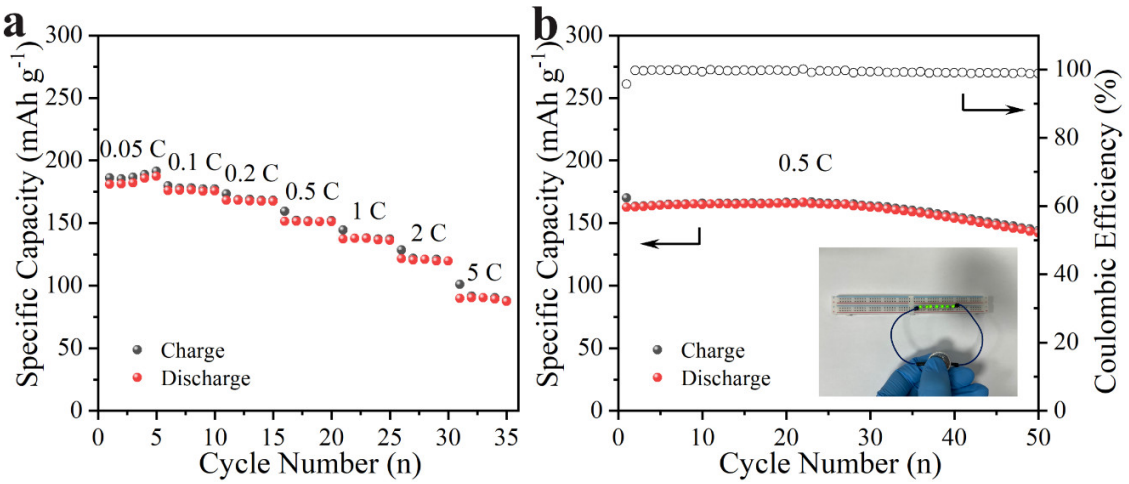

Figure S15. Rate capability at various rates (1 C = 160 mA g^{-1}) (a) and cycling performance (b) of the as-assembled full cell with pre-lithiated PSNs (with the active mass loading of ~0.6 mg cm^{-2}) and $LiCoO_2$ as anode and cathode, respectively. Inset: the digital photograph of light-emitting diode devices lighted up by the full cells.

Table S1 Chemical compositions of clay minerals (wt.%) used in this work.

	SiO_2	Al_2O_3	MgO	CaO	Fe_2O_3	K_2O	Na_2O	MnO	TiO_2	P_2O_5	L. O. I.[a]
Mnt	58.16	16.95	3.57	2.29	5.26	0.15	0.19	0.03	0.20	0.08	13.12
Kln	47.17	37.13	0.38	0.12	0.72	0.60	0.09	<0.01	0.33	0.01	13.02
Hal	41.05	34.97	0.16	0.23	0.30	0.06	0.25	0.03	0.22	<0.01	22.76
Sep	57.45	<0.01	25.20	3.33	1.00	<0.01	0.01	0.01	<0.01	<0.01	13.32

[a] Loss on ignition.

Table S2 Summary of electrochemical performances of 2D nanostructured Si anodes synthesized by various methods in this work and recent studies.

Si anodes	Rate performance	Cycle performance	ICE[a]	Methods	Precursors	Ref.
PSNs	878 mAh g^{-1} at 10 A g^{-1}	1303 mAh g^{-1} at 1.0 A g^{-1} after 500 cycles	85%	Mechanochemical reduction method	Talc	This work
Si nanosheet	1297 mAh g^{-1} at 4.0 A g^{-1}	1576 mAh g^{-1} at 0.4 A g^{-1} after 100 cycles	36%	Magnesiothermic reduction	Mesoporous silica nanosheets from tetraethoxysilane	6
2D Si nanosheets	~652 mAh g^{-1} at 10 A g^{-1}	622 mAh g^{-1} at 2.0 A g^{-1} after 1000 cycles	~70%	Acid washing followed by molten salt-assisted magnesiothermic reduction	Montmorillonite	7
Multiscale hyperporous S flake	~500 mAh g^{-1} at 6.0 A g^{-1}	~700 mAh g^{-1} at 1.5 A g^{-1} after 200 cycles	93%	Molten salt-assisted magnesiothermic reduction	Talc	8
Porous Si nanoplate	950 mAh g^{-1} at 4.2 A g^{-1}	~2278 mAh g^{-1} at 0.21 A g^{-1} after 50 cycles	-	Ion exchange with Mg^{2+} and magnesiothermic reduction	Laponite	9
3D stacked Si nanosheets	700 mAh g^{-1} at 4.0 A g^{-1}	1205 mAh g^{-1} at 0.5 A g^{-1} after 200 cycles	83%	Molten salt-assisted electrochemical reduction	attapulgite	10
2D Si nanosheets	>500 mAh g^{-1} at 40 A g^{-1}	~1500 mAh g^{-1} at 0.4 A g^{-1} after 200 cycles	87%	Chemical vapor deposition by using a NaCl template	Silane	11
2D Si	741 mAh g^{-1} at 5.0 A g^{-1}	835 mAh g^{-1} at 5.0 A g^{-1} after 3000 cycles	70%	Physical vacuum distillation method	Bulk layered calcium−silicon alloy	12
Si nanosheets	600 mAh g^{-1} at 1.0 A g^{-1}	~1400 mAh g^{-1} at 0.2 A g^{-1} after 100 cycles	-	Chemical dealloying method	$Li_{13}Si_4$ alloy	13
Si nanosheets	~400 mAh g^{-1} at 5.0 A g^{-1}	~400 mAh g^{-1} at 1.0 A g^{-1} after 200 cycles	87%	Diamond wire grinding	Silicon ingot	14
Si nanosheets	<50 mAh g^{-1} at 2.0 A g^{-1}	~200 mAh g^{-1} at 0.1 A g^{-1} after 100 cycles	-	DC arc-discharge plasma	Bulk Si	15

[a] Initial Coulombic efficiency

Reference:

1. S. C. Jung, H.-J. Kim, J.-H. Kim and Y.-K. Han, *J. Phys. Chem. C.*, 2016, **120**, 886-892.
2. M. K. Kim, B. Y. Jang, J. S. Lee, J. S. Kim and S. Nahm, *J. Power Sources*, 2013, **244**, 115-121.
3. J. Du, R. L. Zhu, Q. Z. Chen, J. Y. Xie, H. Y. Xian, J. P. Zhang and J. X. Zhu, *Appl. Surf. Sci.*, 2023, **617**, 156566.
4. W. Weppner and R. A. Huggins, *J. Electrochem. Soc.*, 1977, **124**, 1569-1578.
5. X. Zhou, Y. Liu, Y. Ren, T. Mu, X. Yin, C. Du, H. Huo, X. Cheng, P. Zuo and G. Yin, *Adv. Funct. Mater.*, 2021, **31**, 2101145.
6. S. Chen, Z. Chen, X. Y. Xu, C. B. Cao, M. Xia and Y. J. Luo, *Small*, 2018, **14**, 1703361.
7. Y. Ren, L. Xiang, X. Yin, R. Xiao, P. Zuo, Y. Gao, G. Yin and C. Du, *Adv. Funct. Mater.*, 2022, **32**, 2110046.
8. J. Ryu, D. Hong, M. Shin and S. Park, *ACS Nano*, 2016, **10**, 10589-10597.
9. K. Adpakpang, S. B. Patil, S. M. Oh, J.-H. Kang, M. Lacroix and S.-J. Hwang, *Electrochim. Acta*, 2016, **204**, 60-68.
10. Q. Yu, J. Liu, Y. Liang, T. Liu, Y. Zheng, Z. Lai, X. Liu, J. Chen, Q. Zhang and X. Li, *Electrochim. Acta*, 2022, **422**, 140515.
11. J. Ryu, T. Chen, T. Bok, G. Song, J. Ma, C. Hwang, L. Luo, H.-K. Song, J. Cho, C. Wang, S. Zhang and S. Park, *Nat. Commun.*, 2018, **9**, 2924.
12. Y. L. An, Y. Tian, C. L. Wei, H. Y. Jiang, B. J. Xi, S. L. Xiong, J. K. Feng and Y. T. Qian, *ACS Nano*, 2019, **13**, 13690-13701.
13. J. L. Lang, B. Ding, S. Zhang, H. X. Su, B. H. Ge, L. H. Qi, H. J. Gao, X. Y. Li, Q. Y. Li and H. Wu, *Adv. Mater.*, 2017, **29**, 1701777.
14. J. Lu, Y. Zhang, X. Gong, L. Li, S. Pang, G. Qian, Z. Wang and J. Liu, *Chem. Eng. J.*, 2022, **446**, 137022.
15. J. Liang, F. Huo, Z. Zhang, W. Yang, M. Javid, Y. Jung, X. Dong and G. Cao, *Appl. Surf. Sci.*, 2019, **476**, 1000-1007.